Estimated Global Hydrographic Variability

GAËL FORGET AND CARL WUNSCH

Department of Earth, Atmospheric and Planetary Sciences, Massachusetts Institute of Technology, Cambridge, Massachusetts

(Manuscript received 15 February 2006, in final form 25 August 2006)

ABSTRACT

An estimate is made of the three-dimensional global oceanic temperature and salinity variability, omitting the seasonal cycle, both as a major descriptive element of the ocean circulation and for use in the error estimates of state estimation. Historical hydrography, recent data from the World Ocean Circulation Experiment, and Argo profile data are all used. Root-mean-square vertical displacements in the upper 300 m of the ocean are generally smaller than 50 m, except in energetic boundary currents and in the North Atlantic subpolar gyre. Variability in temperature and salinity is strongly correlated below the top 100 m. Salinity contributions to sea surface height variability appear more significant at low latitudes than expected, possibly resulting from advective and diffusive processes. Results are generally consistent with altimetric variability under two simple kinematic hypotheses, and much of the observed structure coincides with known dynamical features. A large fraction of the sea surface height variability is consistent with the hypothesis of dominance of the first baroclinic mode.

1. Introduction

Oceanic baroclinic variability is an essential element of the ocean circulation, and its structures depict many of the elements requiring dynamical explanation. Many estimates of the baroclinic variability already exist (e.g., Wunsch 1997, 1999; Roemmich and Cornuelle 1990; McPhaden et al. 1998; Lysne and Deser 2002; Willis et al. 2004; Dickson et al. 1996; Stammer and Wunsch 1999), showing the fields to be weakly nonstationary in time, strongly nonstationary in space, anisotropic, and involving a wide variety of processes. A synthesis of spectral analyses based on satellite and in situ observations can be found in Zang and Wunsch (2001), who proposed a general wavenumber–frequency spectrum for the ocean interior. None of these previous studies is either comprehensive or global, and some suppressed parts of the signal by filtering. Here a new global estimate is made using both historical and recent hydrographic data, as well as the Argo profile data (Roemmich et al. 2001). This estimate explicitly includes eddy signals, and its main purpose is to provide a major piece of descriptive oceanography, for example, to provide maps of rms vertical displacements in the global ocean.

Two applications of the new global estimate are also discussed. First, the results permit additional tests of general circulation models with eddy resolution below the ocean surface (e.g., see Stammer et al. 1996; Smith et al. 2000). Second, one can better weight instantaneous temperature and salinity observations in least squares fitting problems that focus on the large-scale ocean state [e.g., Estimating the Circulation and Climate of the Ocean (ECCO); Wunsch and Heimbach (2006)].

2. Sources of information, hypotheses, and methodology

We start from a set of sample variances,

$$\overline{\sigma_p^2} = \frac{1}{n_p - 1} \sum_m (X_{p,m} - \overline{X}_p)^2,$$

computed by Stephens et al. (2002) using "historical" data. Here p indexes groups of values; each group is the ensemble of measurements [of temperature (T) or salinity (S)] collected within a $1^\circ \times 1^\circ$ horizontal box. Also, m indexes the n_p individual measurements composing the group, and $\overline{X}_p$ is the sample mean. The sample variance $\overline{\sigma_p^2}$ is used only if $n_p \geq 4$. This latter modest requirement is very restrictive in practice, particularly in the Southern Hemisphere (see Fig. 1). A

Corresponding author address: Dr. Gaël Forget, Department of Earth, Atmospheric and Planetary Sciences, Massachusetts Institute of Technology, Room 54-1516, 77 Massachusetts Avenue, Cambridge, MA 02139.
E-mail: gforget@mit.edu

DOI: 10.1175/JPO3072.1

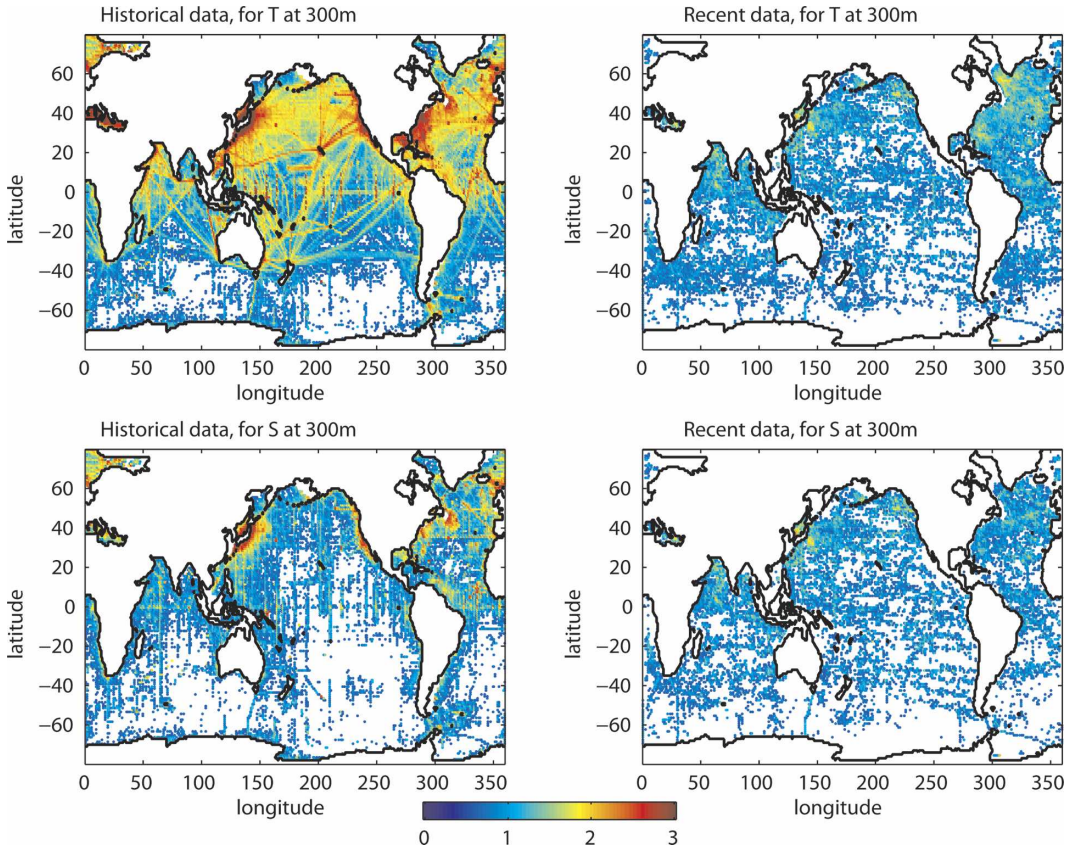

FIG. 1. Number of observations (N) per 1° × 1° box, where it exceeds 4, plotted as $\log_{10}(N)$.

discussion of the reliability of the climatological means (Stephens et al. 2002; Gouretski and Koltermann 2004, and others) is an important issue, but is beyond our present scope. Note, however, the great scarcity in the historical dataset (Fig. 1) of temperature in the Southern Hemisphere, and salinity almost everywhere.

A second set of sample variances ($\overline{\sigma_p^2}$) is computed from the World Ocean Circulation Experiment (WOCE) CTD and Argo profiles (both hereinafter referred to as "recent" data), vertically interpolated to the levels used by Stephens et al. (2002). Most of the Argo profiles have been obtained after 2002. Although the number of observations per year is larger in the recent dataset than in the historical one, the historical data do provide more total overall observations (Fig. 1). The spatial coverage of the recent data is more homogeneous, particularly in salinity coverage (Figs. 1 and 2). In all cases, however, coverage decreases rapidly with depth (Fig. 2) and this drop-off is a major issue (Argo profilers sample neither the near surface nor the region below 2000 m).

Close to the surface, the mean seasonal cycle often has a relatively large amplitude, and here we want to focus on the other contributions to the variability. Therefore, in the first 100 m, we use the historical data grouped by month of the year; the sample variance computed within 1 of these 12 groups omits the variance from the mean seasonal cycle. Similarly, the recent dataset was split into six 2-month groups. Between 100 and 1000 m, we use the 1- or 2-month groups only for grid points where at least one of them includes more than four values; otherwise, we use the data over the entire year.

To begin, the overall variability (the mean seasonal cycle being omitted) here is assumed to be dominated by high-frequency signals (mesoscale eddies, internal waves, front movements, . . .) and to be temporally stationary, so that averaging variance estimates computed over different periods is an acceptable first approximation. Previous analyses of the sea surface height (SSH) variability spectra (Stammer 1997; Zang and Wunsch 2001) support an assumption of mesoscale dominance of kinetic energy. The results of Stammer et al. (2006) suggest that neglecting interannual and seasonal modulation of eddy energy is a reasonable first approximation. This working hypothesis cannot be rigorously correct everywhere, but investigating the partition between climate and eddy signals depending on location is

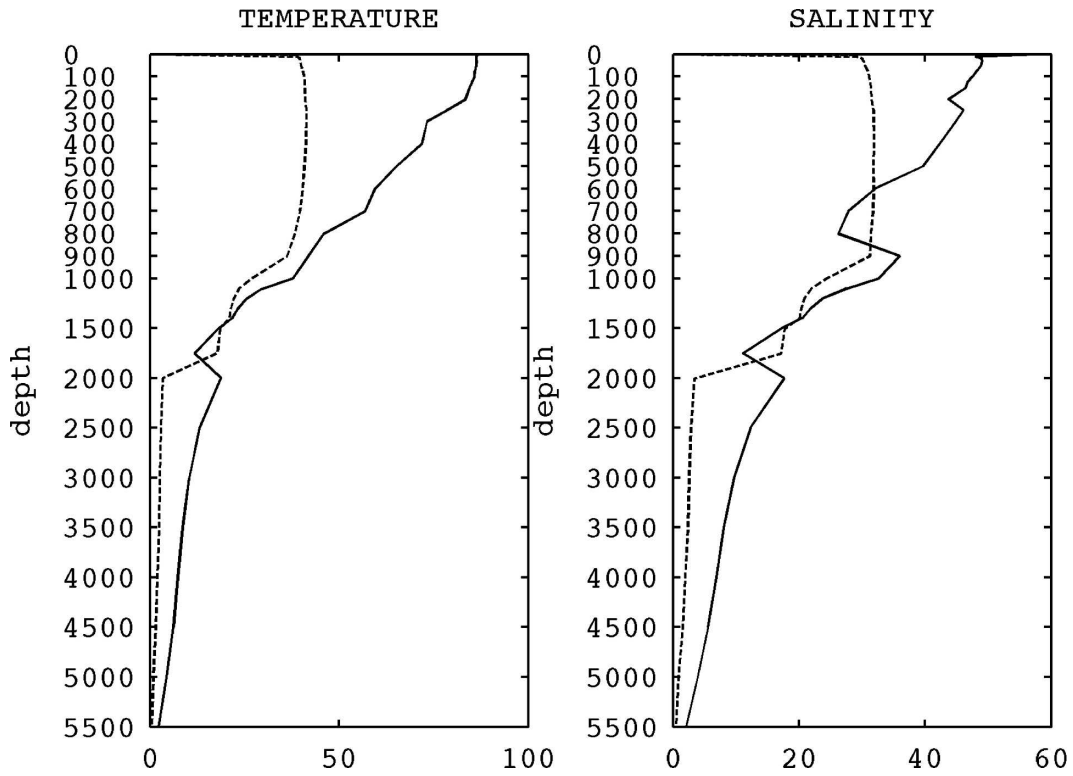

FIG. 2. Percentage of the grid points where a variance estimate can be made, i.e., where the number of observations exceeds 4, for the historical (solid line) and the recent (dashed line) data.

left for further investigation, and will probably necessarily rely on the future accumulation of Argo observations.

The next step is to combine the two sets of sample variance estimates. Let $G_p(i, j)$ be a spatial weighting function defined as

$$G_p(i,j) = \exp\{-[l_p - l(i,j)]^2/r_l - [L_p - L(i,j)]^2/r_L^2 - [\overline{T}_p - \overline{T}(i,j)]^2/r_{\overline{T}}^2 - [\overline{S}_p - \overline{S}(i,j)]^2/r_{\overline{S}}^2\}, \quad (1)$$

where l and L are longitude and latitude, and r_l and r_L are associated decorrelation scales, both taken as 5°. The p subscripted values are those for the box where σ_p is computed, whereas i and j are indices in the $1° \times 1°$ grid. The $\overline{T}$ and $\overline{S}$ terms in Eq. (1) are employed to stretch the weighting function parallel to the contours of T and S. The addition of these terms implies a preferential mapping along the climatological contours, and a reduction of effective decorrelation scales when compared with the 5° background value (e.g., across dynamical structures, such as a sloping thermocline or boundary currents). The relationships between instabilities and the mean flow structure (e.g., see Gill 1982; Stammer 1997, his Fig. 3), and the link between mean tracer distributions and advection motivated this choice, $r_{\overline{T}}$ and $r_{\overline{S}}$, are chosen as the local standard deviation of the climatological mean temperature ($\overline{T}$) and salinity ($\overline{S}$) over the four neighboring grid points. If provided with reliable prior uncertainties and correlation scales for oceanic variances, a minimum variance–mapping method (e.g., Bretherton et al. 1976) would be preferred in future investigations to the ad hoc correlation operator used here. Stephens et al. (2002) used an analogous method to estimate $\overline{T}$ and $\overline{S}$, but with a simpler form of $G_p(i, j)$. The combined variance is then,

$$\overline{\sigma^2}(i,j) = \sum_p G_p(i,j)\overline{\sigma_p^2} n_p/N(i,j), \quad \text{where}$$
$$N(i,j) = \sum_p G_p(i,j) n_p, \quad (2)$$

where the sum on p is taken over the previously computed (historical and recent data) sample variance estimates. Each vertical level is treated independently, leading to three-dimensional fields of variance $\overline{\sigma^2}$ for T and S that are generally illustrated below as $\overline{\sigma} = (\overline{\sigma^2})^{1/2}$, the associated fields of standard deviation (or variability amplitude).

3. An illustration

First, Fig. 3 (upper left) shows the pointwise average of the sample estimates for T at 300 m. This variance average is computed as in Eq. (2), but using $G_p(i, j) = \delta_p(i, j) = \delta[l(i, j) - l_p, L(i, j) - L_p]$, where δ is the

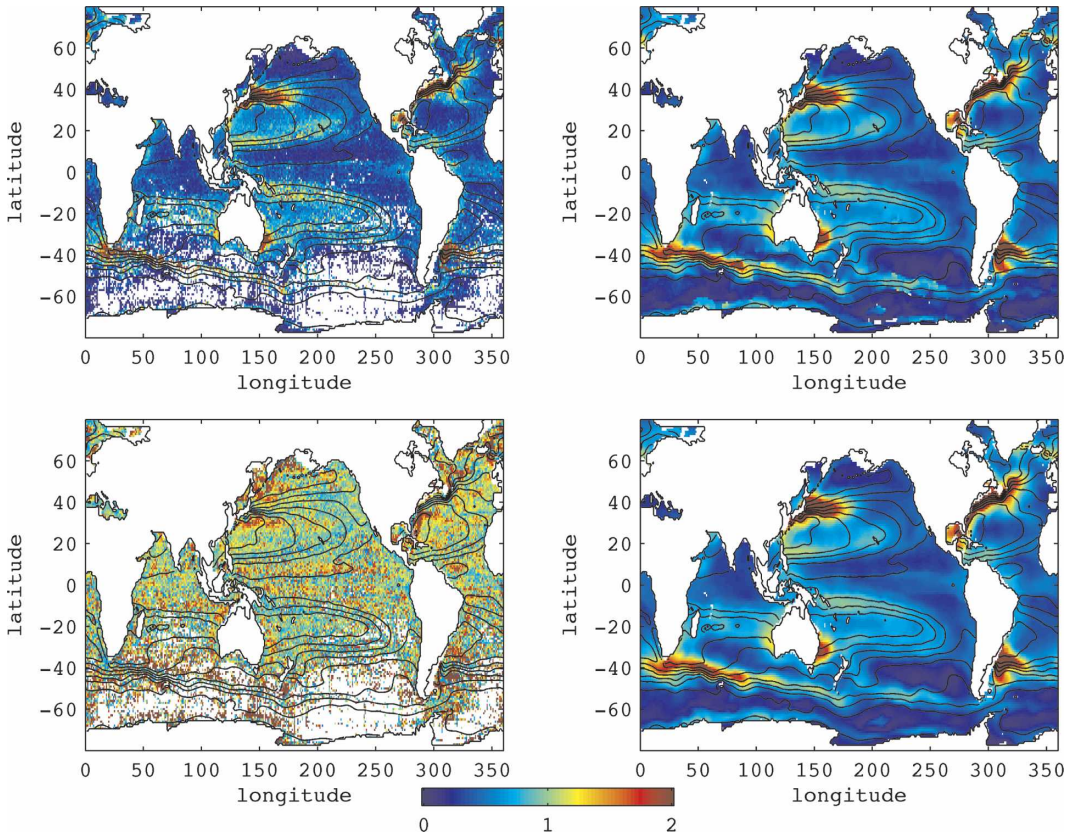

FIG. 3. Illustration of the methodology (see text) for T at 300 m: (top left) pointwise, (top right) mapped, and (bottom right) estimated standard deviations of T (°C); and (bottom left) the ratio of the mapped to the pointwise standard deviations. Superimposed contours: annual mean climatological T ($\overline{T}$) from Stephens et al. (2002) with an interval of 2°C.

Kronecker delta, instead of the nonlocal mapping defined by Eq. (1). First, it shows large-scale structures and a visually obvious relation with the mean horizontal contours and dynamical structures. Second, the noise at the grid scale argues for doing some smoothing, even in the Northern Hemisphere. Third, interpolation is required to obtain the large-scale structure of $\overline{\sigma}_p$ in the much more poorly sampled Southern Hemisphere.

An estimate of the reliability of the estimates is necessary. Assume that the underlying temperature and salinity variables X are normal with variance σ_X^2. Then, a sample variance estimate for X based upon n measurements is chi-square distributed with variance $2 \times \sigma_X^4/(n-1)$, and $n-1$ degrees of freedom (e.g., see Cramér 1946). Applying the relation $\mathrm{var}(aX + bY) = a^2\mathrm{var}(X) + b^2\mathrm{var}(Y)$, one has

$$\mathrm{var}[\overline{\sigma^2}(i,j)] = 2\sum_p \langle \delta_p(i,j)\left\{n_p \Big/ \left[\sum_q \delta_q(i,j)n_q\right]\right\}^2 \Big/ (n_p - 1)\rangle \sigma(i,j)^4, \tag{3}$$

where var is the variance and δ is the Kronecker delta.

Because $\mathrm{var}(Y^{1/2}) \approx \sigma_Y^2/(2\mu_Y^{1/2})^2$ for Y, a random variable (here $Y = \overline{\sigma^2}$) of mean μ_Y and variance σ_Y^2, the approximate standard error estimate for the sample standard deviation ($\overline{\sigma}$), is

$$\mathrm{std}[\overline{\sigma}(i,j)] \approx \left(0.5\sum_p \left\langle \delta_p(i,j)\left\{n_p \Big/ \left[\sum_q \delta_q(i,j)n_q\right]\right\}^2 \Big/ (n_p - 1)\right\rangle\right)^{0.5}\overline{\sigma}(i,j), \tag{4}$$

where std is the standard deviation.

Relative uncertainties, defined as $\mathrm{std}(\overline{\sigma})/\overline{\sigma}$ from Eq. (4), are less than 10% in well-observed areas, and reach 40% in the Southern Hemisphere (Fig. 4, upper). Ab-

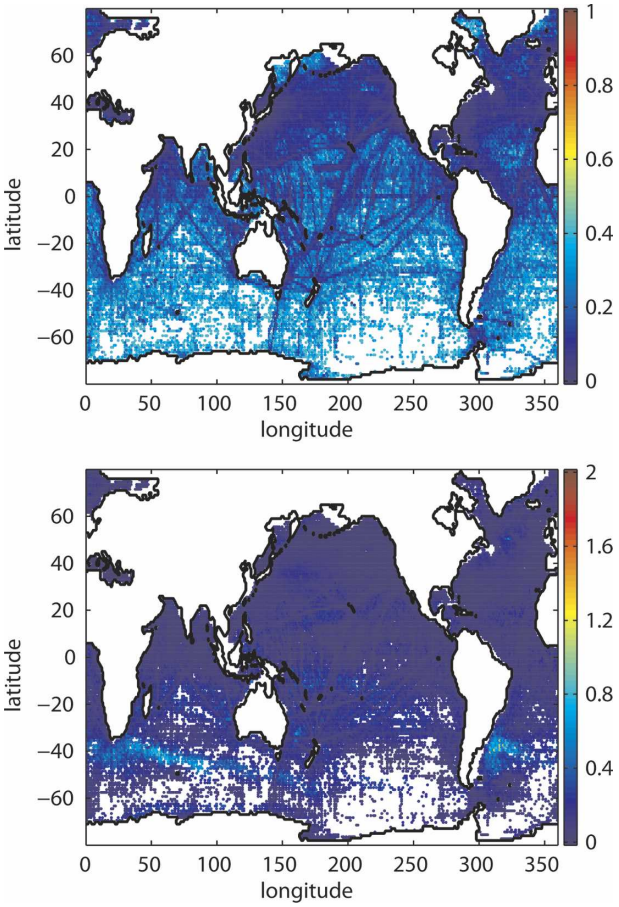

FIG. 4. (top) Relative and (bottom) absolute uncertainty for T at 300 m, defined from Eq. (4) as std($\overline{\sigma}$)/$\overline{\sigma}$ and std($\overline{\sigma}$), respectively.

solute uncertainties, defined as std($\overline{\sigma}$) from Eq. (4), are generally small (Fig. 4, lower), except in the Antarctic Circumpolar Current (ACC) and in the convergence area near the east coast of South America, where $\overline{\sigma}(i, j)$ is large (Fig. 3, upper left) and the sampling is poor (Fig. 1).

The sample variance estimates are now combined using the nonlocal mapping defined by Eq. (1) (Fig. 3, upper right). This field has no visible grid-scale noise, and the original large-scale structure is preserved in the well-sampled areas and seems to emerge in the Southern Ocean. Mapping errors have not been directly estimated; to obtain some measure of reliability, Fig. 3 (lower left) displays the ratio of the pointwise to the mapped variability amplitude. This ratio is generally close to one, suggesting that the mapping has not introduced significant artificial structures, although the smoothing erodes some contrasts (e.g., see the minima of $\overline{\sigma}$ near energetic currents). The correlation coefficient between pointwise and mapped values is 0.84. Values both at grid points with no sample estimate and that are filled by the mapping (Fig. 3, upper panels; e.g., in the Southern Ocean) must be more uncertain than the best-constrained neighboring values, even though omission errors cannot be quantified.

To produce an even smoother field in areas that lack observations, the final estimate (Fig. 3, lower right) is obtained in two additional steps: the mapping of Eq. (1) is applied a second time to fill in a few remaining holes (see Fig. 3, upper right), based upon the surrounding, previously mapped values (which are unchanged in this second calculation); and a third application of the mapping function is then made, globally, to further smooth the result. Although this approach appears draconian and somewhat arbitrary, it produces an aesthetically acceptable result and it has very little effect on the previously mapped values; the point correlation between the final and intermediate mapped values is 0.98.

4. Observed variability

Although each depth level is mapped separately, sections showing the final estimate of the temperature variability rms amplitude ($\tilde{\sigma}_T$) display vertically coherent patterns (Fig. 5). One sees the expected large variability in the major western boundary currents and in the ACC, but Fig. 5 shows these variability maxima to be homogeneously large over the depth range associated with the large horizontal gradients of $\overline{T}$, rather than surface intensified. This feature does not result from the different treatment of the mean seasonal cycle in the 0–100- and 100–1000-m layers, because it persists when we use only 1- or 2-month groups of data homogeneously over the 0–1000-m layer (not shown). An exception is the *jump* in $\tilde{\sigma}_T$ at 100 m in the ACC in the Indian Ocean section that might be spurious (Fig. 5, upper left). A second global feature is the vertical maximum of variability associated with the uppermost stratification maximum at low and midlatitudes, usually referred to as the equatorial and the ventilated (after Luyten et al. 1983) thermocline, respectively. Both of these features appear in the interannual variance profiles computed by Lysne and Deser (2002) for the North Pacific Ocean (see their Figs. 4, 5, and 14) from the historical data.

Variability in the ACC typically ranges between 0.6° and 1.4°C, but exceeds 1.4°C in most of the Indian Ocean downstream of the Agulhas Current retroflection (Fig. 3). The variability amplitude reaches 2.7°C within the Gulf Stream and 3.1°C within the Kuroshio and in the South Atlantic Ocean convergence area. The upper-ocean thermocline variability maximum peaks at the equator, where it ranges from 1.4° to 2.6°C (Fig. 5). In addition to this vertical maximum, the sections of $\tilde{\sigma}_T$

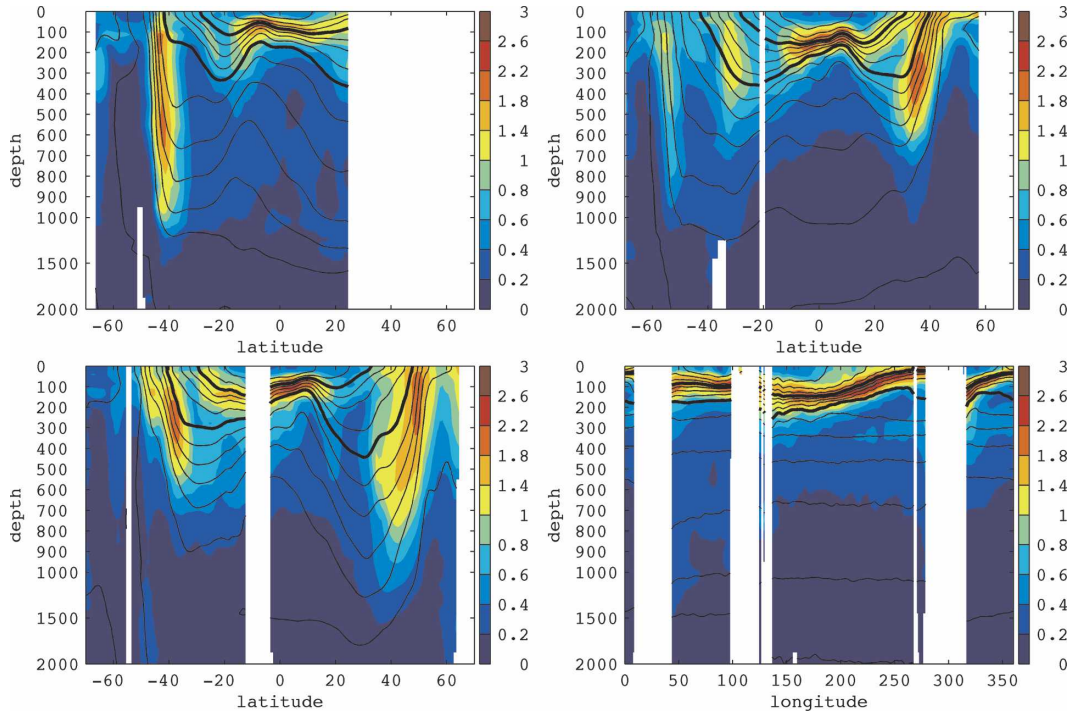

FIG. 5. Estimated standard deviation of T ($\tilde{\sigma}_T$; °C; colors) in (top left) the Indian Ocean at 64.5°E, (top right) the Pacific Ocean at 164.5°E, (bottom left) the Atlantic Ocean at 322.5°E, and (bottom right) along the equator at 0.5°S. Superimposed contours: $\overline{T}$, with an interval of 2°C. Thick contours denote the $\overline{T}$ = 14°C and $\overline{T}$ = 22°C isotherms.

show an ambient variability between 0.2° and 0.4°C down to the deepest part of the thermocline (typically at 1000-m depth).

To summarize the geographic structure of the variability, consider only the $\overline{T}$ = 14°C and $\overline{T}$ = 22°C isotherms (Fig. 6) that are in the lower and central parts of the equatorial maximum variability, respectively (Fig. 5). For the 14°C isotherm (Fig. 6), regional variability maxima link the midlatitude eastern boundaries to the Tropics, and coincide with ventilated thermocline deepening. Eastern Tropics and subtropical gyre interiors correspond to regional variability minima. For the 22°C isotherm (Fig. 6) the tropical maximum variability (typically larger than 1.8°C) covers the global ocean in a band of over 20° of latitude.

Define the local vertical gradients of temperature and salinity as $|\mathrm{grad}_z \overline{T}(z)|$, and so on. Then, multiplying these gradients by a standard vertical displacement (17 m is convenient) produces maps of the temperature and salinity variations expected from a pure, spatially homogeneous vertical displacement. The result is shown in Fig. 7, and, between 30°S and 30°N, correlates with the observed variability amplitude (Fig. 6) up to 0.8 and 0.85 for the 14° and 22°C isotherms, respectively. The stratification is key to understanding the regional contrasts of the variability amplitude, which is likely dominated by vertical displacements. Consequently, the variability of the rms amplitude maps yields rms vertical displacements maps (section 5).

The salinity variability rms amplitude ($\tilde{\sigma}_S$) shows structures very similar to those for temperature (Figs. 8 and 6). For example, both $\tilde{\sigma}_S$ and $\tilde{\sigma}_T$ have subtropical minima where the isotherm deepens. The most striking exception is the absence of a maximum for $\tilde{\sigma}_S$ at 5°N in the Pacific, where a strong vertical gradient exists below the ITCZ in $\overline{T}$, but not in $\overline{S}$. At midlatitudes, zonal sections (Fig. 9) illustrate that most of the contrasts between the $\tilde{\sigma}_S$ and $\tilde{\sigma}_T$ maps can also be associated with contrasts between the (vertical or horizontal) gradients of $\overline{S}$ and $\overline{T}$. In general, the variability is more surface intensified for S than for T up to midlatitudes (Fig. 9), consistent with the results of Maes et al. (2002) close to the equator. For latitudes equatorward of 60°, the correlation between $\tilde{\sigma}_T$ and $\tilde{\sigma}_S$ in the upper layers (5–137 m) is only 0.4, whereas it is 0.9 in the 137–2000-m depth range.

5. Vertical displacement and sea surface height variations

The present maps can be used to make a global assessment of the baroclinic displacements by using

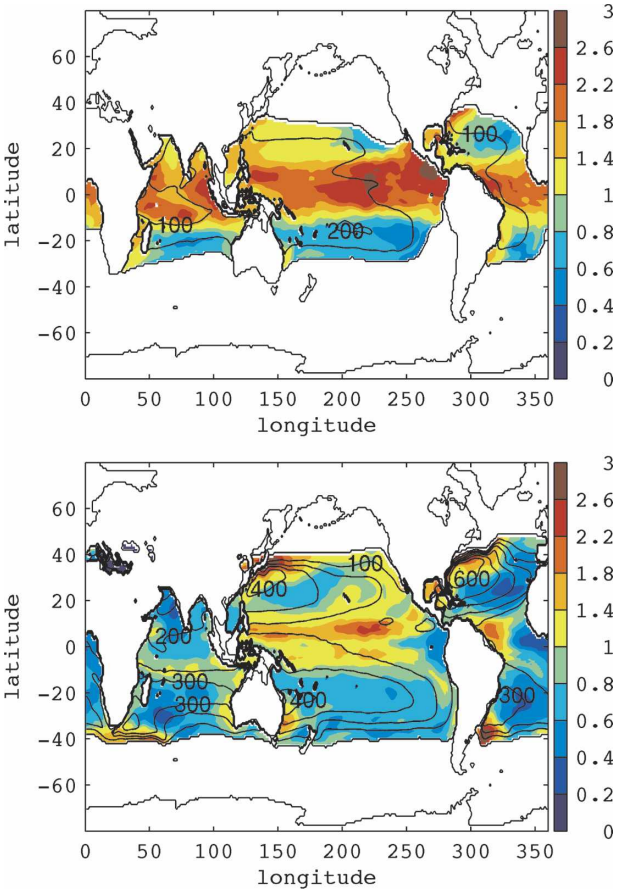

FIG. 6. Here, $\tilde{\sigma}_T$ (°C; colors) on surfaces of constant $\overline{T}$, for (bottom) $\overline{T}$ = 14°C and (top) $\overline{T}$ = 22°C. Superimposed contours: depth of the isotherm, with a contour interval of 100 m.

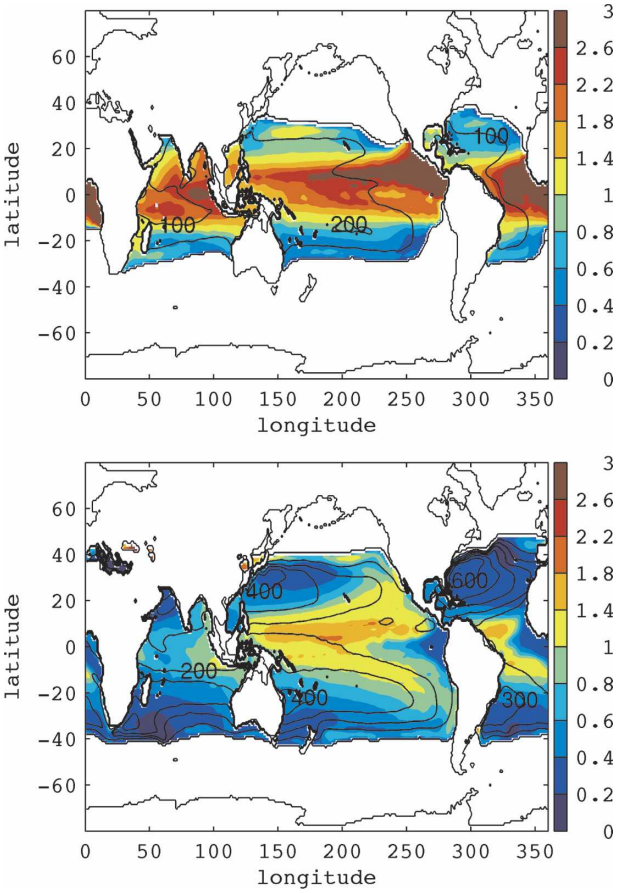

FIG. 7. Same as Fig. 6, but for $|\text{grad}_z\overline{T}| \times dz_0$, where dz_0 is 17 m.

$\tilde{\sigma}_T(z)/|\text{grad}_z\overline{T}(z)|$ and $\tilde{\sigma}_S(z)/|\text{grad}_z\overline{S}(z)|$, where the vertical derivatives are obtained from the climatology. Vertical displacements are first estimated by a standard least squares fit of the $|\text{grad}_z\overline{T}(z)|$ profile to the $\tilde{\sigma}_T(z)$ profile over a depth range rather than at individual vertical levels, and similarly for S. Following the choices of Wunsch (1999), the 0–350- and 350–1000-m layers are considered. Vertical displacements of fluid parcels have to imply variability in both tracers, so the final estimate of rms vertical displacements (Fig. 10) is the minimum of the estimates computed from $\tilde{\sigma}_T$ and from $\tilde{\sigma}_S$ separately.

In the upper layer (Fig. 10) vertical displacements are smaller than 50 m, except in the energetic current systems (where they can exceed 100 m) and in the North Atlantic subpolar gyre. The homogeneity in the Tropics and subtropics (with values between 10 and 20 m) is consistent with the strong similarity of Figs. 6 and 7 noted above. Conversely, for the 14°C isotherm, including latitudes poleward of 30° where larger vertical displacements exist, the correlation between $\tilde{\sigma}_T(z)$ and $|\text{grad}_z\overline{T}(z)|$ is reduced to 0.4. Vertical displacements are generally larger in the lower layer than in the upper one (Fig. 10). This increase is consistent with the Wentzel–Kramers–Brillouin–Jeffreys (WKBJ) approximation (e.g., see Gill 1982) in which vertical displacement in-

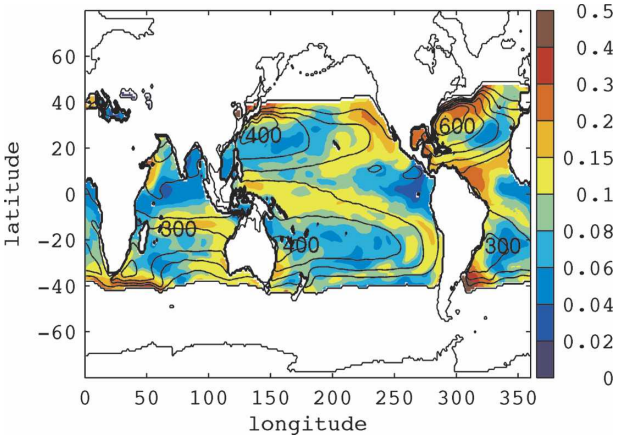

FIG. 8. Estimated standard deviation of S ($\tilde{\sigma}_S$) on the 14°C isotherm. Superimposed contours: depth of the isotherm with an interval of 100 m.

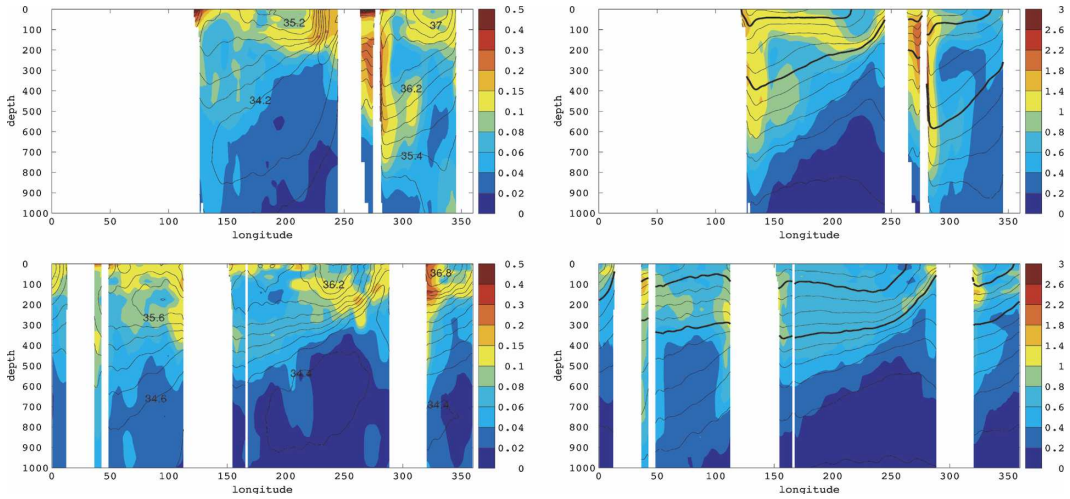

FIG. 9. Estimated standard deviation of (left) S ($\tilde{\sigma}_S$) and (right) T ($\tilde{\sigma}_T$) at (top) 27.5°N and (bottom) 23.5°S. Superimposed contours: $\overline{S}$ with an interval of 0.2 (left), or $\overline{T}$ with an interval of 2°C (right).

creases as the stratification decreases. For both layers, the consistency with the North Atlantic study of Wunsch (1999, his Fig. 1), based on completely independent data, suggests that the present estimates of vertical displacements, and indirectly $\tilde{\sigma}_T$ and $\tilde{\sigma}_S$, are robust in the well-sampled areas. Moreover, in the tropical Pacific, the estimate for the upper layer is in good agreement with the regional results of Maes et al. (2002, their Fig. 4b). The values larger than 50 m below 300 m south of the ACC are more questionable, given the sampling (Fig. 1), even though they occur at almost all longitudes.

Sea surface height change is the sum of baroclinic and barotropic process contributions (e.g., see Wunsch and Stammer 1998). A baroclinic contribution to SSH variability can be inferred from $\tilde{\sigma}_T$ and $\tilde{\sigma}_S$. A first method is to project $\tilde{\sigma}_T$ onto the first baroclinic mode for pressure $\overline{P}_1(z)$ derived (e.g., see Gill 1982) from the climatology (Stephens et al. 2002). Through the hydrostatic approximation, pressure perturbations are related to temperature perturbations:

$$\overline{\sigma_{dP/dz}} = g[\rho(\overline{T} - \tilde{\sigma}_T/2, \overline{S}) - \rho(\overline{T} + \tilde{\sigma}_T/2, \overline{S})].$$

The $d\overline{P}_1/dz$ profile (of constant sign) is fit to the $\overline{\sigma_{dP/dz}}$ profile to obtain a variability amplitude $a_{1,T}$ for the first mode $\overline{P}_1(z)$ at each horizontal grid point. Last, $\overline{\sigma}_{\mathrm{SSH},1,T} = a_{1,T}/(\rho_0 g)\overline{P}_1(z = 0)$ is the SSH variability amplitude (Fig. 11, upper panel), which is generally in good agreement with rms(SSH) variability computed from altimeter data (e.g., see Wunsch and Stammer 1998, their Fig. 8a). Values ranging from 30 to 50 cm are found for the Gulf Stream, the Kuroshio, and the South Atlantic convergence area, and for the ACC in the In-

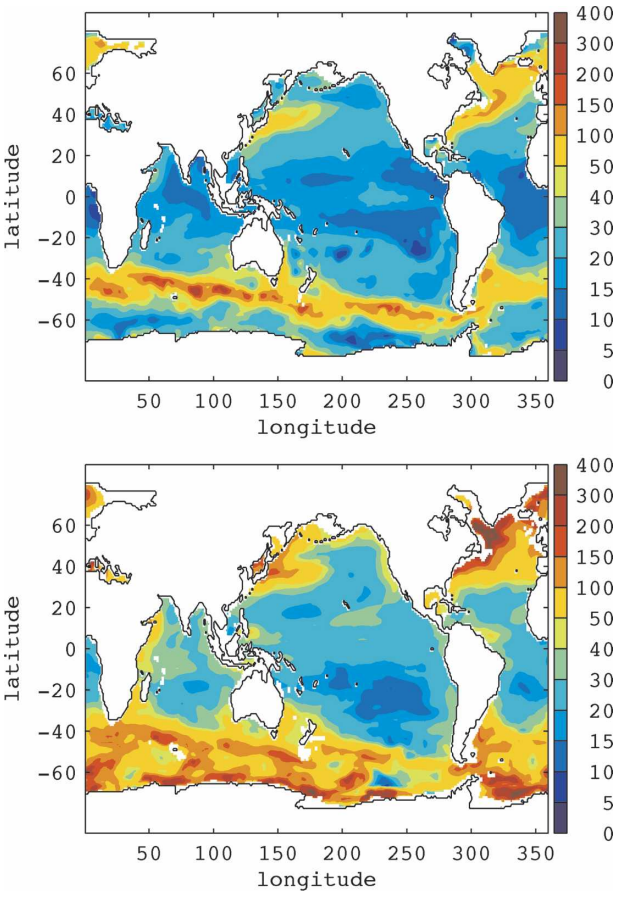

FIG. 10. Root-mean-square vertical displacements (m) inferred (see text) from $\tilde{\sigma}_T$ and $\tilde{\sigma}_S$ for the (top) 5–350- and (bottom) 350–1050-m layers.

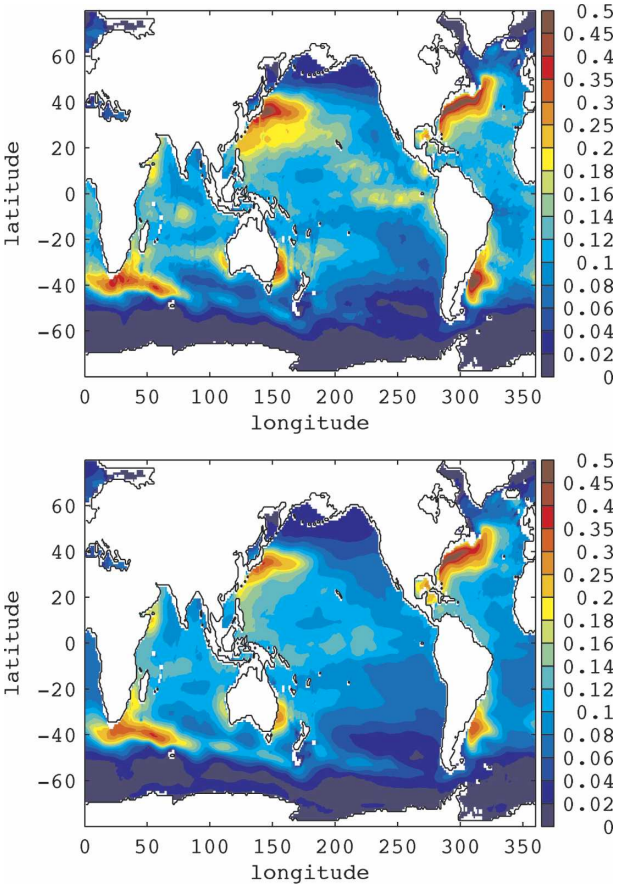

FIG. 11. Variability of sea surface height (m) inferred from $\tilde{\sigma}_T$ using two different methods (see text): (top) $\overline{\sigma}_{\mathrm{SSH},1,T}$ and (bottom) $\overline{\sigma}_{\mathrm{SSH,int},T}$.

dian basin. The minimum (<10 cm) just north of the ACC in the Indian Ocean, the maxima close to the Australian east and west coasts, and the minima in the eastern Pacific subtropical basins (<8 cm) are other examples of consistent patterns. This agreement with the altimeter data (Wunsch and Stammer 1998), both for amplitudes and geographic contrasts, suggests that interpreting the SSH variability as the signature of the first baroclinic mode is a reasonable approximation, consistent with the results of Wunsch (1997) for kinetic energy.

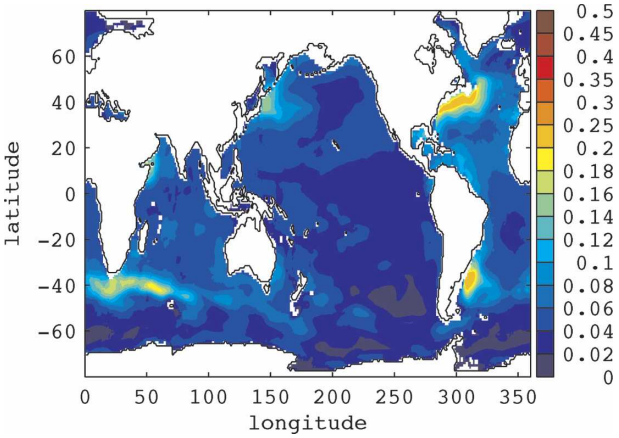

FIG. 12. Variability of sea surface height ($\overline{\sigma}_{\mathrm{SSH,int},S}$; m; see text) inferred from $\tilde{\sigma}_S$.

A second method to infer SSH variability from $\tilde{\sigma}_T$ consists of a direct integration under the hydrostatic and Boussinesq approximations,

$$\overline{\sigma}_{\mathrm{SSH,int},T} = 1/(\rho_0 g)\int_{-d}^{0} \overline{\sigma_{dP/dz}}\, dz,$$

where d is the depth at which $\overline{P}_1$ reverses sign, which typically is between 1000 and 2000 m (not shown). Interpreting this computation as the variability of SSH relies on the following two assumptions: 1) for $z > d$, density variations at all depths are strictly in phase, and

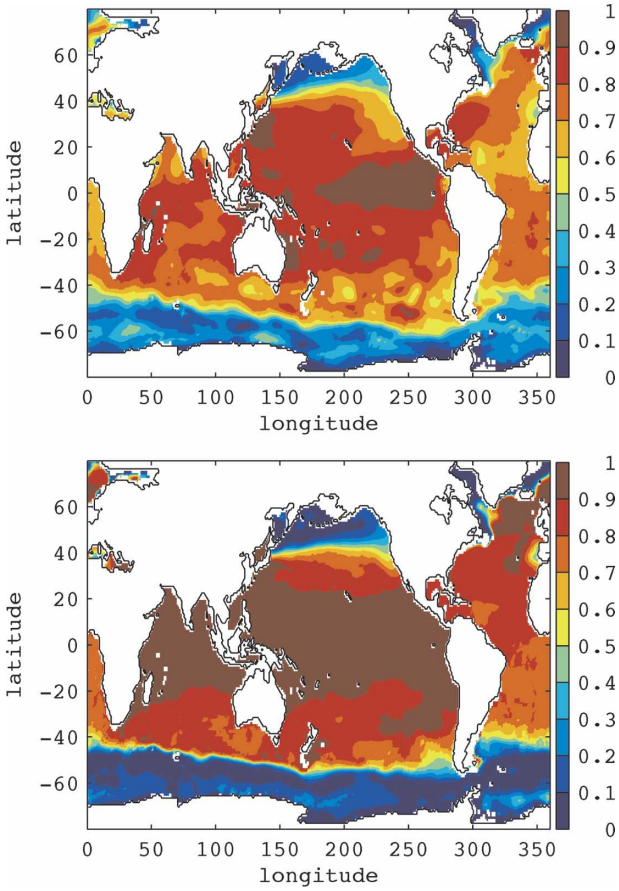

FIG. 13. (top) Variance ratio $\overline{\sigma}^2_{\mathrm{SSH,int},T}/(\overline{\sigma}^2_{\mathrm{SSH,int},T} + \overline{\sigma}^2_{\mathrm{SSH,int},S})$ and (bottom) analogous ratio for first baroclinic mode vertical displacements $D_1(z)$. The two computations differ only by the use of $|\mathrm{grad}_z \overline{T}(z) \times D_1(z)|$ and $|\mathrm{grad}_z \overline{S}(z) \times D_1(z)|$ in the bottom panel instead of $\tilde{\sigma}_T$ and $\tilde{\sigma}_S$, which are used in the top panel.

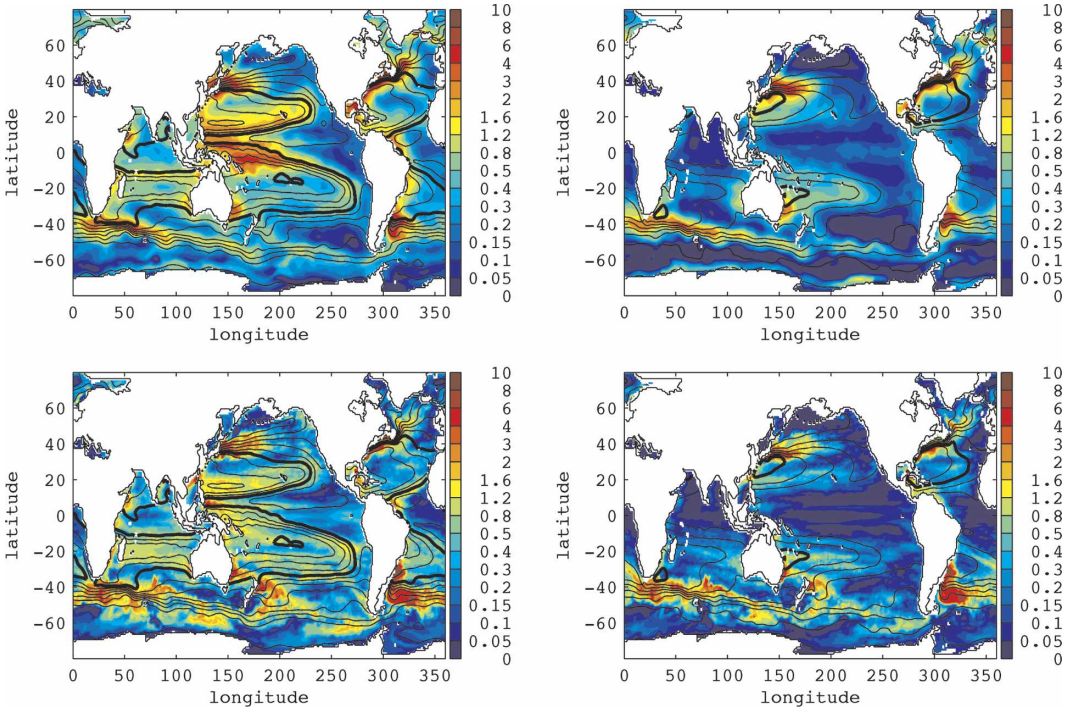

FIG. 14. Variance of T at (left) 200 and (right) 400 m (°C^2) (top) as estimated from the data ($\tilde{\sigma}_T^2$) and (bottom) as simulated by an eddy-resolving model (σ_m^2).

2) at d, the pressure anomalies vanish (no anomalous motion). These two assumptions are reasonable to the extent that the first baroclinic mode dominates the motions. Under assumption 1 solely, this method corresponds to a steric height variability computation (e.g., see Gilson et al. 1998). The correlation of 0.9 between $\overline{\sigma}_{\mathrm{SSH},1,T}$ and $\overline{\sigma}_{\mathrm{SSH,int},T}$ illustrates the general consistency of this integral computation with the first mode fit. However, $\overline{\sigma}_{\mathrm{SSH},1,T}$ and $\overline{\sigma}_{\mathrm{SSH,int},T}$ are sensibly different in some regions (e.g., in the eastern tropical Pacific, in the eastern Atlantic, and in the ACC), revealing inconsistencies between the vertical structures of the first baroclinic mode and the observed variability amplitude ($\tilde{\sigma}_T$). In the densely sampled region, detectable contributions of higher modes, or other processes (e.g., mixing or lateral advection) in $\tilde{\sigma}_T$, are the most likely explanation of these differences.

The SSH variability $\overline{\sigma}_{\mathrm{SSH,int},S}$ inferred from $\tilde{\sigma}_S$ is generally small (Fig. 12), typically a few centimeters, except in the western boundary current systems where it is close to 20 cm. Consistent with the conventional picture, the contribution of S to the SSH variability can be neglected to first order in the Tropics and subtropics, but dominates at higher latitudes (Fig. 13). Nevertheless, when we account for the observed variability amplitude (upper) rather than for the mean stratification (lower), salinity contributions become less negligible at low and midlatitudes. This result again suggests detectable contributions from mixing and lateral advection.

6. Comparison with an eddy-resolving model

One of the reasons for constructing compilations such as this one is their use in testing general circulation models with eddy resolution (e.g., see Stammer et al. 1996; Smith et al. 2000). Here we briefly compare our present estimates with a 1/8° global model simulation (Hill et al. 2007). Because the maps constructed here are based upon a number of assumptions and a fragmentary dataset, the comparison, if favorable, begins to lend verisimilitude both to the eddy statistics and the model.

The model is forced with 6-hourly wind stresses, heat fluxes, and freshwater fluxes obtained from the National Centers for Environmental Prediction–National Center for Atmospheric Research (NCEP–NCAR) reanalysis project from 1992 to 2002 (Kalnay et al. 1996), and the results were stored as 10-day averages. Twelve standard deviation fields are computed from the 10-day averages over the last 8 yr of the simulation and are grouped by month of the year. Then, σ_m is estimated as the average of these 12 fields, which are finally averaged horizontally and interpolated vertically onto the grid of Stephens et al. (2002). Consistent with the data

estimate, the mean seasonal cycle is thus omitted and the seasonal cycle of eddy energy is neglected.

For latitudes below 60° and in the 0–2000-m depth range, the correlation between σ_m and $\tilde{\sigma}$ is 0.8 for T and 0.7 for S. The maps (Fig. 14) for T at 200 and 400 m illustrate the overall agreement between the simulated (lower panels) and observed (upper panels) variability, both in the localization and in the amplitude. One difference is found in the western Pacific Tropics where the model variability maximum is shallower than 200 m (not shown). Resulting from eddy contributions, the present model–data comparison is fundamentally different from that of Lysne and Deser (2002) in the North Pacific, who focus on climate signals and show much weaker variability estimates derived from annual mean fields (from the historical dataset and a 1° resolution model).

7. Cost function computation

A primary motivation for the present calculations is the need to construct cost functions for oceanic state estimation (e.g., Wunsch and Heimbach 2006). Cost functions are typically written as sums of terms of the form $J = [\mathbf{y}(t) - \mathbf{E}(t)\mathbf{x}(t)]^{\mathrm{T}}\mathbf{W}(t)[\mathbf{y}(t) - \mathbf{E}(t)\mathbf{x}(t)]$, where $\mathbf{y}(t)$ is a vector of data at time t, $\mathbf{x}(t)$ is the model state vector, and $\mathbf{W}(t)$ is a weight matrix. Here, $\mathbf{E}(t)$ is a matrix mapping the model elements into the observations; $W_{i_1 i_1}$ is commonly, but not necessarily, defined as $1/\sigma^2_{\mathrm{err}}$, where σ^2_{err} is the combined model and data error variance for component i_1. The notation provides for use of a full-weight matrix $\mathbf{W}$, but we do not yet have any useful information on off-diagonal hydrographic weights.

Because eddies generally dominate the overall oceanic variability and their energy varies geographically (e.g., see Stammer 1997; Zang and Wunsch 2001), σ_{err} must be spatially heterogeneous when measuring the difference between either a model or a climatology [e.g., here Stephens et al. (2002)] and any instantaneous measurement (e.g., here Argo profiles). In the present case, we choose $\sigma_{\mathrm{err}}(i, j, k) = \tilde{\sigma}(i, j, k)$. If the unscaled difference between the Argo profiles and the climatology is used, the difference (Fig. 15, lower) is spatially very heterogeneous, but when normalized, as shown, the differences (Fig. 15, upper) are much more uniform.

In a cost function using $\tilde{\sigma}_T$ and $\tilde{\sigma}_S$, observations are consistently downweighted in regions of high eddy activity. However, low-frequency contributions to $\tilde{\sigma}_T$ and $\tilde{\sigma}_S$ are regarded as errors in such a cost function, and σ_{err} should eventually be reevaluated. This particularly applies to the tropical Pacific, where ENSO actually dominates the total variability (e.g., Kessler et al. 1996).

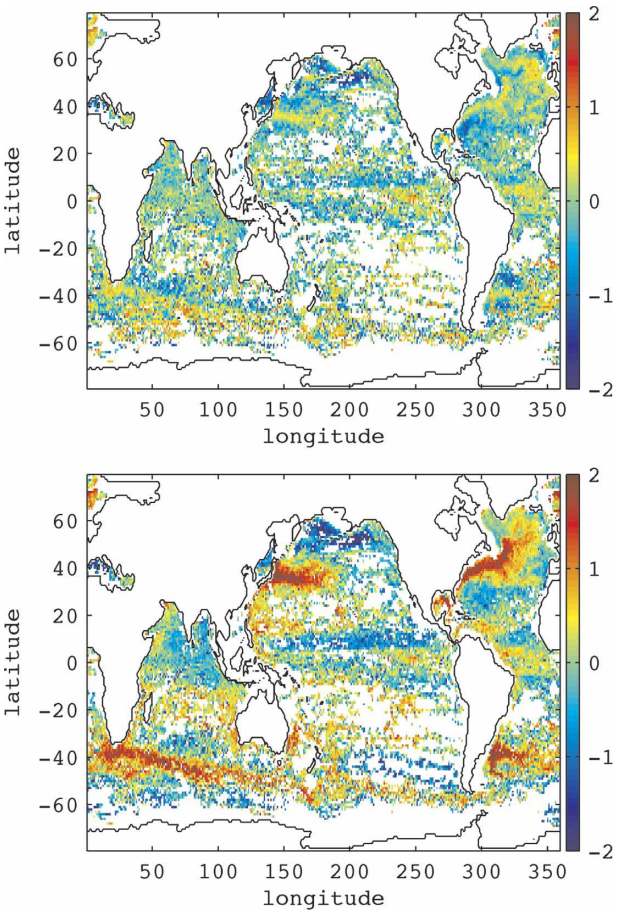

FIG. 15. Distance [$\log_{10}(J)$; see text] between the Argo data available from 2002 to 2005 and the monthly climatology of Stephens et al. (2002) for T at 300 m, on average for each grid point, for two definitions of J (see text): (top) $\sigma_{\mathrm{err}}(i, j, k) = \tilde{\sigma}_T(i, j, k)$ and (bottom) $\sigma_{\mathrm{err}}(i, j, k) = \sigma_{\mathrm{err}}(k)$ is spatially homogeneous, with $\sigma_{\mathrm{err}}(k) = \mathrm{mean}_{ij}[\tilde{\sigma}_T(i, j, k)]$.

8. Discussion

A three-dimensional global estimate has been made of the baroclinic variability (omitting the mean seasonal cycle) of T and S, based on the historical datasets and the recent hydrographic and Argo measurements. The estimate shows a strong geographical resemblance to mean dynamical structures, particularly in the western boundary currents and the thermocline at mid- and low latitudes. The Argo observations permit improved global estimates of salinity variability. As expected, temperature and salinity variability display a strong resemblance to each other, except in the upper 100 m.

Vertical displacements inferred from the T and S variability are consistent with the North Atlantic results of Wunsch (1999). Estimated amplitudes for the 0–350-m depth range are generally smaller than about 50 m, except in energetic currents and the North At-

lantic subpolar gyre. For the 350–1050-m depth range, vertical displacements are generally larger, consistent with the WKBJ approximation (e.g., see Gill 1982). SSH variability amplitude maps inferred from the baroclinic variations are generally quantitatively consistent with the altimeter observations. Over the global ocean, the interpretation of the SSH variability as the vertical displacement signature of the first baroclinic mode is a reasonable approximation. As expected, the contribution of S to the SSH variability can be neglected to first order in the Tropics and subtropics, but it is dominant toward the poles. Detectable contributions from mixing and lateral advection are, however, present.

Future Argo observations are expected to greatly improve the present estimates above 2000 m and the statistical description of T and S variability in general, first by simply increasing the amount and size of samples. Moreover, improved large-scale state estimates will enable a more precise focus on eddy signals computed as residual misfits. Because a state estimation system, including model dynamics (e.g., see Wunsch and Heimbach 2006), can efficiently isolate the large-scale signals from sets of even very noisy profiles (Forget et al. 2007), the present estimates can themselves contribute to these future improvements through a better formulation of state estimation problems.

Acknowledgments. This work was supported by the National Ocean Partnership Program (NOPP), with funds from the National Aeronautics and Space Administration and the National Ocean and Atmospheric Administration to the ECCO-GODAE Consortium. We thank our many ECCO partners for their support.

REFERENCES

Bretherton, F., R. Davis, and C. Fandry, 1976: A technique for objective analysis and design of oceanographic experiments applied to MODE-73. *Deep-Sea Res.,* **23,** 559–582.

Cramér, H., 1946: *Mathematical Methods of Statistics.* Princeton University Press, 575 pp.

Dickson, R., J. Lazier, J. Meincke, P. Rhines, and J. Swift, 1996: Long term coordinated changes in the convective activity of the North Atlantic. *Progress in Oceanography,* Vol. 38, Pergamon Press, 241–295.

Forget, G., B. Ferron, and H. Mercier, 2007: Combining Argo profiles with a general circulation model in the North Atlantic. Part 1: Estimation of hydrographic and circulation anomalies from synthetic profiles, over a year. *Ocean Modell.,* in press.

Gill, A. E., 1982: *Atmosphere–Ocean Dynamics.* Academic Press, 662 pp.

Gilson, J., D. Roemmich, B. Cornuelle, and L. Fu, 1998: Relationship of TOPEX/Poseidon altimetric height and circulation in the North Pacific. *J. Geophys. Res.,* **103,** 27 947–27 965.

Gouretski, V., and K. Koltermann, 2004: WOCE global hydrographic climatology. Berichte des Bundesamtes für Seeschiffahrt und Hydrographie Tech. Rep. 35, 52 pp.

Hill, C., D. Menemenlis, B. Ciotti, and C. Henze, 2007: Investigating solution convergence in a global ocean model using a 2048-processor cluster of distributed shared memory machines. *Sci. Programm.,* in press.

Kalnay, E., and Coauthors, 1996: The NCEP/NCAR 40-Year Reanalysis Project. *Bull. Amer. Meteor. Soc.,* **77,** 437–471.

Kessler, W., M. Spillane, M. McPhaden, and D. Harrison, 1996: Scales of variability in the equatorial Pacific inferred from the Tropical Atmosphere–Ocean buoy array. *J. Climate,* **9,** 2999–3024.

Luyten, J., J. Pedlosky, and H. Stommel, 1983: The ventilated thermocline. *J. Phys. Oceanogr.,* **13,** 292–309.

Lysne, J., and C. Deser, 2002: Wind-driven thermocline variability in the Pacific: A model–data comparison. *J. Climate,* **15,** 829–845.

Maes, C., M. McPhaden, and D. Behringer, 2002: Signatures of salinity variability in tropical Pacific Ocean dynamic height anomalies. *J. Geophys. Res.,* **107,** 8012, doi:10.1029/2000JC000737.

McPhaden, M., and Coauthors, 1998: The Tropical Ocean-Global Atmosphere observing system: A decade of progress. *J. Geophys. Res.,* **103,** 14 169–14 240.

Roemmich, D., and B. Cornuelle, 1990: Observing the fluctuations of gyre-scale ocean circulation: A study of the subtropical South Pacific. *J. Phys. Oceanogr.,* **20,** 1919–1930.

——, and Coauthors, 2001: Argo: The global array of profiling floats. *Observing the Oceans in the 21st Century,* C. J. Koblinsky and N. R. Smith, Eds., GODAE Project Office and Bureau of Meteorology, 248–258.

Smith, R., M. Maltrud, F. F. O. Bryan, and W. M. W. Hecht, 2000: Numerical simulation of the North Atlantic Ocean at ⅒°. *J. Phys. Oceanogr.,* **30,** 1532–1561.

Stammer, D., 1997: Global characteristic of ocean variability estimated from regional TOPEX/Poseidon altimeter measurements. *J. Phys. Oceanogr.,* **27,** 1743–1770.

——, and C. Wunsch, 1999: Temporal changes in eddy energy of the oceans. *Deep-Sea Res.,* **46,** 77–108.

——, R. Tokmakian, A. Semtner, and C. Wunsch, 1996: How well does a 1/4° global circulation model simulate large-scale oceanic observations? *J. Geophys. Res.,* **101,** 25 779–25 812.

——, C. Wunsch, and K. Ueyoshi, 2006: Temporal changes in ocean eddy transports. *J. Phys. Oceanogr.,* **36,** 543–550.

Stephens, C., J. I. Antonov, T. P. Boyer, M. E. Conkright, R. A. Locarnini, T. D. O'Brien, and H. E. Garcia, 2002: *Temperature.* Vol. 1, *World Ocean Atlas 2001,* NOAA Atlas NESDIS 49, 167 pp.

Willis, J. K., D. Roemmich, and B. Cornuelle, 2004: Interannual variability in upper ocean heat content, temperature, and thermosteric expansion on global scales. *J. Geophys. Res.,* **109,** C12036, doi:10.1029/2003JC002260.

Wunsch, C., 1997: The vertical partition of oceanic kinetic energy. *J. Phys. Oceanogr.,* **27,** 1770–1794.

——, 1999: A summary of North Atlantic baroclinic variability. *J. Phys. Oceanogr.,* **29,** 3161–3166.

——, and D. Stammer, 1998: Satellite altimetry, the marine geoid and the oceanic general circulation. *Annu. Rev. Earth Planet. Sci.,* **26,** 219–253.

——, and P. Heimbach, 2006: Estimated decadal changes in the North Atlantic meridional overturning circulation and heat flux 1993–2004. *J. Phys. Oceanogr.,* **36,** 2012–2024.

Zang, X., and C. Wunsch, 2001: Spectral description of low-frequency oceanic variability. *J. Phys. Oceanogr.,* **31,** 3073–3095.